Micelle Heterogeneity from the 2D Kinetics of Solute Rotation

Jason R. Darvin and Mark A. Berg*

Department of Chemistry and Biochemistry, University of South Carolina, Columbia, SC 29208, USA

*Email: berg@sc.edu

Subject Category: Chemical and Dynamical Processes in Solution; Polymers, Glasses, and Soft Matter

ABSTRACT

The chemical and physical properties of microstructured materials vary with position. The photophysics of solute molecules can measure these local properties, but they often show multiple rates (rate dispersion), which complicates the interpretation. In the case of micelles, rate dispersion in a solute's anisotropy decay has been assigned to either local anisotropy or heterogeneity in the local viscosity. To resolve this conflict, the rotation of PM597 molecules in SDS micelles has been measured by polarized MUPPETS (multiple population-period transient spectroscopy). This 2D technique shows that heterogeneity is strong and that local anisotropy is minimal. The results suggest that on a subnanosecond timescale, the solute sees only one strong fluctuation of the micelle structure. The anisotropic, average structure only emerges on longer timescales.

TOC GRAPHIC

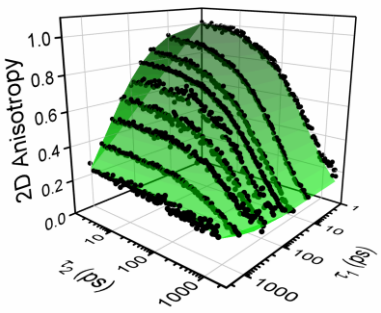

KEYWORDS

ultrafast spectroscopy, multidimensional spectroscopy, complex dynamics, surfactants, dispersed kinetics

In soft, microstructured materials—micelles, vesicles, gels, star polymers, polymer nanoparticles, and so on—there are intertwined questions of where a solute resides and what local properties it sees. The photophysics of a solute that is also a chromophore are often used to gain information.[1-27] Static (0D) measurements, for example, the fluorescence quantum yield or Stokes' shift, give a spatial average of static properties, such as hydrogen-bond availability or polarity. Time-resolved measurements with one time dimension (1D) give rates that characterize dynamic properties. For example, the reorientation or solvation rate characterizes the local viscosity or dielectric-relaxation time, but again, only with an average over locations. In microstructure materials, these 1D kinetics often have nonexponential decays. The implications are clearly important, but the cause is often ambiguous. This Letter shows how 2D kinetics[28-39] resolve this problem. MUPPETS (multiple population-period transient spectroscopy)—a 2D version of ultrafast optical spectroscopy;[37-39]—is applied to micelles to distinguish between different pictures of the solute distribution and the local properties of a micelle.

The rotation time of a dye-molecule solute can be measured by the decay of its optical anisotropy.[40] It is well established that the rotation time reflects the solvent's macroscopic viscosity. In simple solvents, the decay is close to a single exponential, yielding a single viscosity. (Deviations are seen, even in pure solvents, when complexity is added, for example, slow solvation,[41] oligomeric solvents,[38, 41-42] or ionic liquids.[43]) When the same experiment is performed in microstructured materials in general, and micelles in particular, the anisotropy decays become nonexponential and appears to have multiple rates.[16-27] (Whether this rate dispersion should be described as a multiexponential (discrete rates) or as a stretched exponential or other continuous rate distribution is not experimentally decidable, but depends on the model used to describe it. We use a nonparametric approach that does not distinguish between these cases.[34])

A simple explanation for the observed rate dispersion is that it reflects rate heterogeneity.[9, 14-15, 23] Solute molecules occupy a variety of positions within the micelle, and these positions have different local viscosities. Each solute has a specific microviscosity, a well-defined rotation time, and an exponential anisotropy decay, but 1D kinetics only see the average over the distribution of microviscosities. In this model, the distribution of observed rates can be directly converted into a distribution of viscosities.

A contrasting, but widely accepted,[16-22, 24-27] explanation is the "wobble-in-a-cone" model.[44-46] This model is homogeneous. It assumes that every micelle has the average structure, which is strongly layered into a hydrocarbon core, a surface layer of partially hydrated head groups, and the aqueous solvent. It further assumes that the probe is confined to the surface layer, and this layer is strongly anisotropic. As a result, the solute can only "wobble" over a restricted cone of angles about the local director. Other angles are explored more slowly by diffusion to a different point on the surface. In its simplest form, this model predicts a biexponential decay: the fast time gives

the viscosity of the surface layer, the slow time gives the layer's diffusion constant, and the relative amplitude is related to the cone angle. Every molecule experiences both fast and slow processes in sequence, and the rates seen on one molecule are also seen on every other molecule. Using 1D kinetics alone, it is difficult, if not impossible, to distinguish between the wobble-in-a-cone and heterogeneity models.

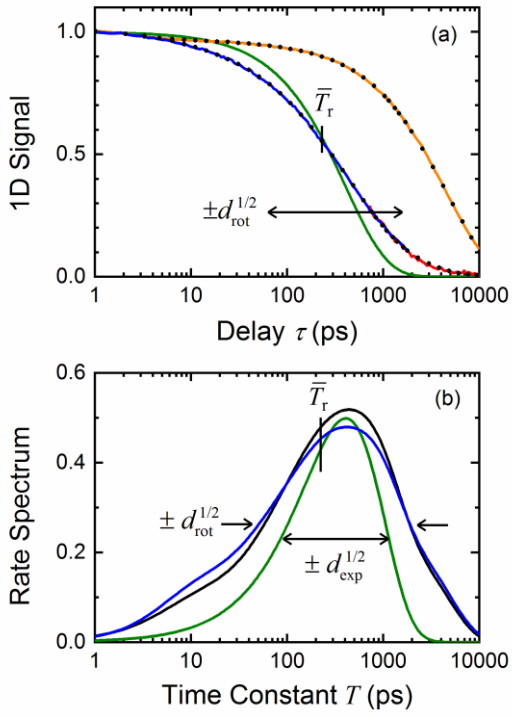

Figure 1. The 1D kinetics of PM597 in SDS micelles. (a) The rotational decay $C_r^{(1)}(\tau)$ from pump–probe measurements (blue) and time-correlated single-photon counting (red) is shown as a solid curve. The nonexponential rotational dynamics are characterized by the geometric-mean time $\bar{T}_r$ and the rate dispersion d_{rot}. A single exponential with the same $\bar{T}_r$ (green) and its own dispersion d_{exp} is shown for comparison. A smooth fit (black dots) is used to produce the spectrum in (b). The rotation-free electronic decay $C_e^{(1)}(\tau)$ (orange) is also shown with its smooth fit (black dots). (b) Rotational decay spectra from 1D (black) and 2D (blue) measurements.

The 1D kinetics of pyrromethene 597 (PM597)[47-49] in sodium-dodecyl-sulfate (SDS) micelles[50-55] are shown in Figure 1. The absorption change with parallel $\Delta A_{\parallel}(\tau)$ and perpendicular $\Delta A_{\perp}(\tau)$ polarizations are converted to the electronic,

$$C_e^{(1)}(\tau) = \frac{\frac{1}{3}\Delta A_{\parallel}(\tau) + \frac{2}{3}\Delta A_{\perp}(\tau)}{\frac{1}{3}\Delta A_{\parallel}(0) + \frac{2}{3}\Delta A_{\perp}(0)} \qquad (1)$$

and rotational,

$$C_{\mathrm{r}}^{(1)}(\tau)=\frac{\Delta A_{\parallel}(\tau)-\Delta A_{\perp}(\tau)}{\frac{5}{9}\Delta A_{\parallel}(\tau)+\frac{10}{9}\Delta A_{\perp}(\tau)} \tag{2}$$

decays (Figure 1a).[40] [See the Supporting Information (SI) for experimental methods.] The electronic decay is similar to the electronic lifetimes reported for PM597 in other solvents.[47] The rotational decay is also similar to those for other dye molecules in a variety of micelles.[16-27] It is clearly stretched relative to a single exponential. For reference, a stretched-exponential fit ($\exp[(-\tau/T_0)^{\beta}]$, not shown) gives $\beta = 0.66$.

Because different models imply different fitting functions, we analyze the data with a nonparametric approach, that is, one that does not require a specific form for the fitting function.[34] The data is smoothed (see SI) so its derivative can be taken to give the "decay spectrum" (Figure 1b),

$$\hat{C}_{\mathrm{r}}^{(1)}(\ln T)=-\left(\frac{\partial C_{\mathrm{r}}^{(1)}(\tau)}{\partial \ln \tau}\right)_{T=\tau} \tag{3}$$

The first moment of this spectrum gives the geometric-mean rotation time, $\overline{T}_{\mathrm{r}}$ = 230 ps. The second central moment (variance) is the total rate dispersion $d_{\mathrm{rot}} = 3.22$, substantially higher than for a single exponential decay ($d_{\mathrm{exp}} = 1.645$).

This decay spectrum contrasts with the more common rate spectrum $\tilde{C}_{\mathrm{r}}^{(1)}(\ln T)$,

$$C_{\mathrm{r}}^{(1)}(\tau)=\int_{-\infty}^{\infty}\tilde{C}_{\mathrm{r}}^{(1)}(\ln T)\mathrm{e}^{-\tau/T}d(\ln T) \tag{4}$$

which is an inverse-Laplace transform on a log scale. It expresses the rotational decay as a superposition of exponential decays with time constants T. The advantage of the decay spectrum is that it can be derived uniquely from the data, whereas finding the rate spectrum is well-known to be an ill-posed problem without a unique solution.[56] The precise relationship between the decay and rate spectra is

$$\hat{C}^{(1)}=\tilde{C}^{(1)}*\hat{C}_{\mathrm{exp}}^{(1)} \tag{5}$$

where the star indicates convolution on the ln-T scale. Thus, the measurement of the rate spectrum is obscured by a "response function" $\hat{C}_{\mathrm{exp}}^{(1)}(\ln T)$, which is the decay spectrum of an exponential decay (green curve in Figure 1b). It is a precisely known function, but it obscures the details of the rate spectrum nonetheless. Equation 5 shows that the lack of uniqueness in the rate spectrum is the same as the ambiguity in deconvolution. Because variances add under convolution, we can quantify the degree of stretching by the excess rate dispersion d_{exc}, the difference between the variance of the experimental spectrum d_{rot} and the variance of the response function d_{exp}, d_{exc} =

$d_{\mathrm{rot}} - d_{\mathrm{exp}} = 1.58$. Broad features, such as these variances, can be recovered despite the convolution, even though fine features cannot.

A general way to model the dispersion in the rotational decay is to start with a homogenous decay shape $C^{(1)}_{\mathrm{hom}}(\tau / T)$, which is shared by all molecules. For example, it could be the biexponential decay predicted by the wobble-in-a-cone model. It has an excess dispersion d_{hom} or a total dispersion $d_{\mathrm{hom}} + d_{\mathrm{exp}}$. In addition, each molecule may have its own time constant T, which is distributed with a probability $P_{\mathrm{het}}(T)$. Combining this heterogeneous source of rate dispersion with the homogeneous decay give the total decay,

$$C^{(1)}_{\mathrm{rot}}(\tau) = \int_0^\infty C_{\mathrm{hom}}(\tau / T) P_{\mathrm{het}}(T) dT \tag{6}$$

This model assumes that the local time constant does not change during the decay; it is in the slow rate-exchange limit.

With this model,

$$\hat{C}^{(1)}_{\mathrm{r}} = \hat{C}_{\mathrm{hom}} * P_{\mathrm{het}} \tag{7}$$

and

$$d_{\mathrm{rot}} = d_{\mathrm{hom}} + d_{\mathrm{exp}} + d_{\mathrm{het}} \tag{8}$$

where d_{het} is the variance of $P_{\mathrm{het}}(T)$ on a ln-T scale. One-dimensional methods can measure the excess rate dispersion, $d_{\mathrm{exc}} = d_{\mathrm{rot}} - d_{\mathrm{exp}} = d_{\mathrm{hom}} + d_{\mathrm{het}}$, but they provide no means to separate this sum into its components.

Two-dimensional kinetics[28-39] are sensitive to the difference between homogeneous and heterogeneous rate dispersion.[37] In these experiments, there are two excitations of the sample separated by a time interval τ_1. A measurement of the state of the system and its return to equilibrium occurs after a second period τ_2, measured from the second excitation. If the response of the system is nonlinear, this signal differs from the sum of the signals from each excitation individually. This difference is the 2D decay $C^{(2)}(\tau_2, \tau_1)$.

MUPPETS is a version of 2D kinetics based on ultrafast optical excitation of electronic states.[37] Each excitation is a pair of simultaneous laser pulses crossed at the sample to produce a spatial grating of excited states. The final measurement is by heterodyned diffraction from the mixed grating created by the nonlinear interaction of both excitations. This configuration requires a six-pulse sequence, but results in single-shot cancellation of the 1D signals from each excitation acting individually. The optical system used to generate this pulse sequence is described in the SI.

When using polarized pulses, there are four unique correlation functions differing by the type of dynamics measured in each time interval: rotation–rotation, electronic–electronic, symmetric rotation–electronic, and asymmetric rotation–electronic. The first two can be isolated with

measurements at only two polarization combinations: $\Delta A_{++}(\tau_2, \tau_1)$ and $\Delta A_{-+}(\tau_2, \tau_1)$ (see Figure S4a in the SI).[38] These can be added to give the electronic–electronic correlation,

$$C_{\mathrm{ee}}^{(2)}(\tau_2,\tau_1) = \frac{\frac{7}{12}\Delta A_{++}(\tau_2,\tau_1) + \frac{5}{12}\Delta A_{+-}(\tau_2,\tau_1)}{\frac{7}{12}\Delta A_{++}(0,0) + \frac{5}{12}\Delta A_{+-}(0,0)} \tag{9}$$

or subtracted to give the rotation–rotation correlation,

$$C_{\mathrm{rr}}^{(2)}(\tau_2,\tau_1) = \frac{\Delta A_{++}(\tau_2,\tau_1) - \Delta A_{+-}(\tau_2,\tau_1)}{\frac{7}{12}\Delta A_{++}(\tau_2,\tau_1) + \frac{5}{12}\Delta A_{+-}(\tau_2,\tau_1)} \tag{10}$$

The resulting electronic–electronic surface is shown in Figure 2a as a set of slices at fixed τ_1. The 1D decay (Figure 1a) is nearly single exponential. There is an additional small component that is attributed to electronic-state solvation, which causes a spectral shift and a slight drop in cross section at early times. Thus, no heterogeneity is expected. The solid curves are predicted from the 1D electronic decay, making this assumption. The data in Figure 2a do not deviate from the predictions in a systematic way as τ_1 increases. This result indicates that there is no heterogeneity in the electronic-state relaxation. Attention can focus on the more interesting rotational dynamics.

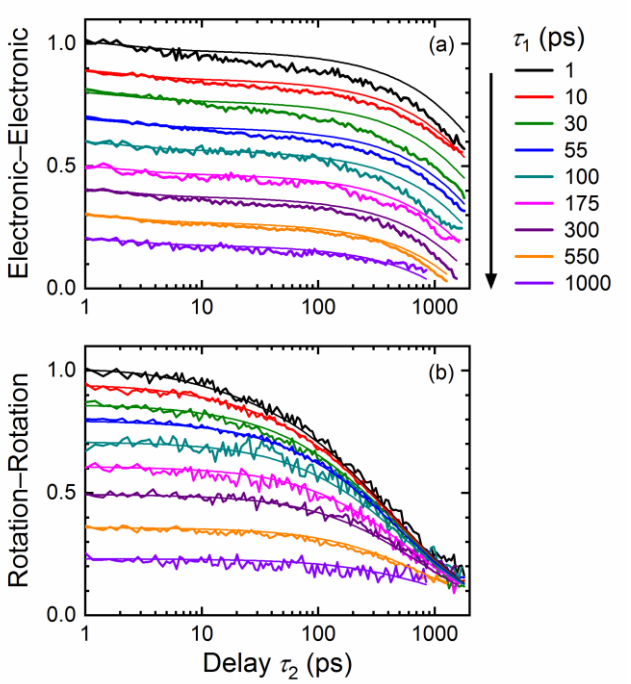

Figure 2. The 2D kinetics of PM597 in SDS micelles. The (a) electronic–electronic $C_{ee}^{(2)}(\tau_2,\tau_1)$ and (b) rotation–rotation $C_{rr}^{(2)}(\tau_2,\tau_1)$ surfaces are shown as a series of cuts at constant τ_1. The smooth curves in (a) are the predictions from the 1D results, assuming a homogeneous electronic decay. In (b), the curves are a smoothing fit. They are used to produce the decay spectra in Figure 3.

The rotation–rotation results are shown in Figure 2b. Careful examination shows that these shapes do change systematically as τ_1 increases; small τ_1 curves begin decaying earlier than curves with a large τ_1. This result indicates that rate heterogeneity is important in the rotational dynamics. For a more quantitative interpretation, the data are smoothed and converted to a 2D decay spectrum (see SI). The smoothing surface is shown as the curves in Figure 2b; the corresponding spectrum is shown in Figure 3b.

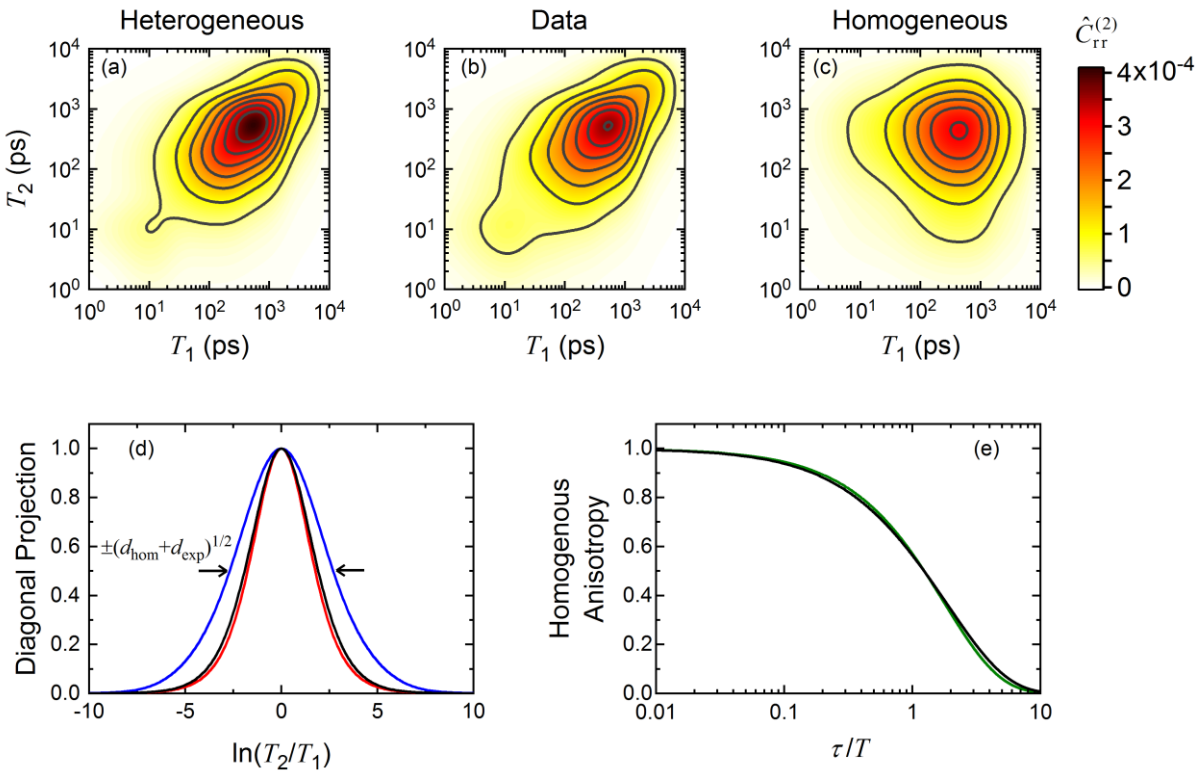

(two-column figure)

Figure 3. Analysis of the rotation–rotation results (Figure 2b). The 2D decay spectra $\hat{C}^{(2)}_{rr}(T_2,T_1)$ for (a) 100% heterogeneity and (c) 0% heterogeneity are compared to (b) the measured spectrum. (d) Projections of the decay spectra along the diagonal: 100% heterogeneous (a, red), measured (b, black) and 0% heterogeneous (c, blue). (e) The decay shape for an individual molecule ($C_{hom}(\tau/T)$, black) compared to an exponential (green).

A 2D decay spectrum indicates the degree of correlation between the time constant T_1 that a molecule has during τ_1 and the time constant T_2 that it has during τ_2. For heterogeneous rate dispersion, each time constant has a distribution throughout the sample; for a specific molecule, there is only one time constant, which is the same in both time intervals. If we could measure the 2D rate spectrum, it would be spread along the diagonal with all the rates of the 1D spectrum, but it would be a delta function along the antidiagonal. However, we can only directly measure the 2D decay spectrum, which is a convolution of the rate spectrum with the spectrum of an exponential (similar to eq 5). Figure 3a shows the decay spectrum calculated from the 1D data, assuming only heterogeneous rate dispersion and including this convolution. Despite the convolution, the elongation along the diagonal is clear.

On the other hand, if the rate dispersion is homogeneous, the various rates seen in the 1D data represent sequential steps in a relaxation process that is experienced by every molecule. Even a single molecule will experience all time constants during two separate relaxation events, one during τ_1 and one during τ_2. In a 2D rate spectrum, there would be off-diagonal "cross peaks" at every combination of time constants. Figure 3c shows the decay spectrum calculated from the 1D data, assuming only homogeneous rate dispersion and including the convolution with the response function. The spectrum is compact with similar widths along the diagonal and the antidiagonal.

The measured 2D decay spectrum (Figure 3b) is strongly elongated, indicating that rate heterogeneity is the primary source of rate dispersion. The same qualitative conclusion can be taken from the time-domain data (Figure 2b), but the 2D spectrum makes it more visually evident.

The 2D spectrum is also easy to quantify. In principle, both local anisotropy and local viscosity variation, that is both homogeneous and heterogeneous mechanisms, may be acting simultaneously. Thus, the quantitative question is what fraction of the rate dispersion is due to rate heterogeneity. Within the slow rate-exchange model (eq 6), the 2D spectrum can be further reduced to two, 1D projections.[34] The integrations involved result in additional averaging of the experimental noise.

If the 2D spectrum is projected along the vertical (or horizontal) axis, it should give the 1D spectrum. This projection from the 2D spectrum (Figure 3b) is compared to the result from the 1D data in Figure 1b. They are in good agreement. (The vertical projections of the heterogeneous and homogeneous models in Figures 3a and 3c agree perfectly with the 1D data, by construction.)

The new information in the 2D spectrum comes from the other projection, which is taken along the diagonal (Figure 3d). It has a variance of $d_{\mathrm{dia}} = d_{\mathrm{hom}} + d_{\mathrm{exp}}$; the heterogeneous contribution in eq 8 is absent.[34] For comparison, the projections of the homogeneous and heterogeneous models (Figures 3a and 3c) are also shown. The data are close to the heterogeneous limit, but there is a slight broadening due to some degree of homogeneous rate dispersion. The effect is small, but eliminating it results in a clear increase in the chi-squared of the fit to the time-domain data (see SI).

The variances of these two projections can be combined to give the fraction of the excess rate dispersion that is due to rate heterogeneity,

$$f_{\mathrm{het}} = \frac{d_{\mathrm{het}}}{d_{\mathrm{hom}} + d_{\mathrm{het}}} = \frac{d_{\mathrm{rot}} - d_{\mathrm{dia}}}{d_{\mathrm{rot}} - d_{\mathrm{exp}}} = 87\% \tag{11}$$

When the projections are reduced to their two variances, there is even more averaging of experimental noise. This single number is a reduction or "averaging" of all the data in Figure 2. Thus, it is more reliable than one might anticipate. It also does not rely on assumptions about the specific mechanism responsible for either the homogeneous or heterogeneous rate dispersion or

using specific functions to represent $C_{hom}(\tau/T)$ or $P_{het}(T)$. It only assumes the general form of eq 6.

Although the 1D data cannot be uniquely decomposed into homogenous and heterogeneous contributions, the loss of information in eq 6 is not complete. The loss primarily affects the high moments of $C_{hom}(\tau/T)$ or $P_{het}(T)$. An example of a decomposition with the correct low moments can be created using the 2D results and mild assumptions. We assign a biexponential to $C_{hom}(\tau/T)$ and a beta distribution to $P_{het}(T)$. The biexponential is the simplest form from the wobble-in-a-cone model for local anisotropy. The beta distribution is a smooth, single peaked function with four adjustable parameters.[57] With these forms, the SI shows that the first four moments of the 1D decay spectrum and the value of f_{het} from the 2D measurements can be correctly reproduced. The resulting inversion of eq 6 correctly represents the major features of $C_{hom}(\tau/T)$ and $P_{het}(T)$, even though the details are not unique.

Figure 3d compares $C_{hom}(\tau/T)$ to a single exponential. This comparison correctly illustrates the magnitude of the homogeneous rate dispersion, which in turn, reflects the amount of anisotropy in the solute's local environment. It is quite small, near the limits of experimental detectability.

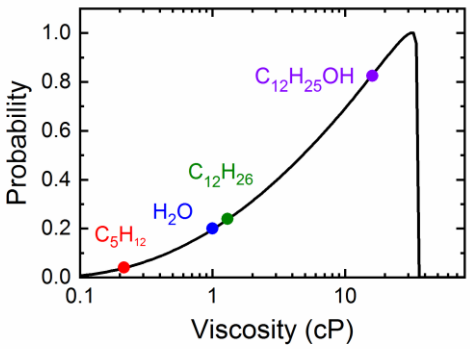

Figure 4. The distribution of microviscosities seen by the solute. The viscosities of several pure solvents are marked for reference.

Figure 4 shows the distribution of microviscosities implied by the measurements. The rotation time of PM597 in several pure solvents was measured to establish the relationship between rotation time and viscosity (SI). This figure must be interpreted with the understanding that finer features may be distorted in the deconvolution. For example, the low viscosity tail may decay too slowly or the high viscosity cut-off may be too sharp. However, the mean position, width and skewness of the distribution are well represented. Thus, microviscosities are significantly populated from levels near, or even below, those of the external water (1 cP) to ones ~30-fold higher. The high

viscosity is not simply characteristic of long hydrocarbon chains: the viscosity of dodecane is only 1.3 cP. Rather it is caused by constraints on the motion imposed by the micelle structure. A similarly high viscosity is found in dodecanol (16.1 cP), where motion is constrained by the need to maintain hydrogen bonding between the sparse hydroxyl groups. The skew is strong, with the peak probability near the maximum microviscosity and a steadily decreasing probability for lower microviscosities. This shape has implications for a structural interpretation.

Many discussions of micelles are based on their average structure. This structure can be seen in measurements that average over many molecules, such as light,[54] x-ray[52] or neutron[51, 53] scattering. In a sense, they are mean-field discussions. The wobble-in-a-cone model adds the idea that a solute is tightly confined to a single portion of this structure, resulting in homogenous behavior.

To create the observed heterogeneity, we could keep the mean-field picture of the micelle, but add a strong radial gradient in microviscosity and assume that take the solutes distribute throughout the micelle. However, the highest viscosity would be in the center, which occupies a small volume. The intermediate region has a larger volume and, as a result, most solutes would be in a region of intermediate microviscosity. The strong skew in Figure 4 is hard to explain.

On the other hand, we can drop the mean-field picture. Micelles are held together by weak forces, allowing large fluctuations in their instantaneous structure. Heterogeneity arises not just from the variety of conditions within one micelle, but also from the diversity of structures from micelle to micelle. Most structures have a substantial region from which water is excluded and where the solute is most soluble. The need to exclude water constrains motion, creating a high viscosity. In the interfacial region, the water, head groups, and hydrocarbon mix in ways that are much more diverse, with more water exposure leading to sites that are more mobile, but also less favorable to the solute. This picture can account for the broad and highly skewed distribution of microviscosities, if the range of instantaneous configurations persist over the nanosecond duration of the measurement.

The same issues are relevant to other microstructured materials and other processes. These materials are all susceptible to large fluctuations in structure that can persist over times longer than important chemical events. The average structure seen in many experiments only becomes relevant on longer timescales. Two-dimensional kinetics offer a direct approach to probing the properties of such fluctuations.

■ ASSOCIATED CONTENT

Supporting Information

The Supporting Information is available free of charge on the ACS Publications website at DOI: *to be inserted*

Experimental methods, nonparametric data reduction, and approximating the microviscosity distribution (PDF)

■ AUTHOR INFORMATION

Corresponding Author

*Email: berg@sc.edu

ORCID

Jason R. Darvin: 0000-0003-4222-7388

Mark A. Berg: 0000-0002-9063-4810

Notes

The authors declare no competing financial interest.

■ ACKNOWLEDGEMENT

This material is based upon work supported by the National Science Foundation under CHE-1707813.

■ REFERENCES

(1) Vyšniauskas, A.; Kuimova, M. K. A Twisted Tale: Measuring Viscosity and Temperature of Microenvironments Using Molecular Rotors. *Int. Rev. Phys. Chem.* **2018**, *37* (2), 259-285.

(2) Demchenko, A. P.; Mély, Y.; Duportail, G.; Klymchenko, A. S. Monitoring Biophysical Properties of Lipid Membranes by Environment-Sensitive Fluorescent Probes. *Biophys. J.* **2009**, *96* (9), 3461-3470.

(3) Levinger, N. E. Ultrafast Dynamics in Reverse Micelles, Microemulsions, and Vesicles. *Curr. Opin. Colloid Interface Sci.* **2000**, *5* (1-2), 118-124.

(4) Ober, K.; Volz-Rakebrand, P.; Stellmacher, J.; Brodwolf, R.; Licha, K.; Haag, R.; Alexiev, U. Expanding the Scope of Reporting Nanoparticles: Sensing of Lipid Phase Transitions and Nanoviscosities in Lipid Membranes. *Langmuir* **2019**, *35* (35), 11422-11434.

(5) Wang, S.; Thorn, A.; Redmond, G. Photophysical Probing of Dye Microenvironment, Diffusion Dynamics, and Energy Transfer. *J. Phys. Chem. C* **2018**, *122* (12), 6900-6911.

(6) Ahmed, S. A.; Gautam, R. K.; Sharma, P.; Seth, D. Photophysics of a Molecular Rotor inside the Block Co-Polymers. *J. Photochem. Photobiol. A* **2018**, *351*, 170-178.

(7) Samanta, P.; Rane, S.; Bahadur, P.; Dutta Choudhury, S.; Pal, H. Tetronic Star Block Copolymer Micelles: Photophysical Characterization of Microenvironments and Applicability for Tuning Electron Transfer Reactions. *J. Phys. Chem. B* **2018**, *122* (22), 6079-6093.

(8) Mukherjee, P.; Das, A.; Sen, P. Ultrafast Excited State Deactivation Channel of Thioflavin T Adsorbed on SDS Micelle: A Combined Femtosecond Fluorescence and Transient Absorption Study. *J. Photochem. Photobiol. A* **2017**, *348*, 287-294.

(9) Neda, D.; Christina, M. O. Temperature Dependent Heterogeneous Rotational Correlation in Lipids. *Phys. Biol.* **2016**, *13* (6), 066004.

(10) Brandt, E. G.; Edholm, O. Stretched Exponential Dynamics in Lipid Bilayer Simulations. *J. Chem. Phys.* **2010**, *133* (11), 115101.

(11) Nojima, Y.; Iwata, K. Viscosity Heterogeneity inside Lipid Bilayers of Single-Component Phosphatidylcholine Liposomes Observed with Picosecond Time-Resolved Fluorescence Spectroscopy. *J. Phys. Chem. B* **2014**, *118* (29), 8631-8641.

(12) Das, R.; Duportail, G.; Richert, L.; Klymchenko, A.; Mély, Y. Sensing Micelle Hydration by Proton-Transfer Dynamics of a 3-Hydroxychromone Dye: Role of the Surfactant Headgroup and Chain Length. *Langmuir* **2012**, *28* (18), 7147-7159.

(13) Bhattacharyya, S.; Paramanik, B.; Patra, A. Energy Transfer and Confined Motion of Dyes Trapped in Semiconducting Conjugated Polymer Nanoparticles. *J. Phys. Chem. C* **2011**, *115* (43), 20832-20839.

(14) Steege, K. E.; Wang, J.; Uhrich, K. E.; Castner, E. W. Local Polarity and Microviscosity in the Hydrophobic Cores of Amphiphilic Star-Like and Scorpion-Like Macromolecules. *Macromolecules* **2007**, *40* (10), 3739-3748.

(15) Parasassi, T.; Conti, F.; Glaser, M.; Gratton, E. Detection of Phospholipid Phase Separation. A Multifrequency Phase Fluorimetry Study of 1,6-Diphenyl-1,3,5-Hexatriene Fluorescence. *J. Biol. Chem.* **1984**, *259* (22), 14011-14017.

(16) Visser, A. J. W. G.; Vos, K.; Van Hoek, A.; Santema, J. S. Time-Resolved Fluorescence Depolarization of Rhodamine B and Octadecylrhodamine B in Triton X-100 Micelles and Aerosol OT Reversed Micelles. *J. Phys. Chem.* **1988**, *92* (3), 759-765.

(17) Quitevis, E. L.; Marcus, A. H.; Fayer, M. D. Dynamics of Ionic Lipophyilic Probes in Micelles: Picosecond Fluorescence Depolarization Measurements. *J. Phys. Chem.* **1993**, *97*, 5762-5769.

(18) Heitz, M. P.; Bright, F. V. Rotational Reorientation Dynamics of Xanthene Dyes within the Interior of Aerosol-OT Reversed Micelles. *Appl. Spectosc.* **1995**, *49* (1), 20-30.

(19) Maiti, N. C.; Krishna, M. M. G.; Britto, P. J.; Periasamy, N. Fluorescence Dynamics of Dye Probes in Micelles. *J. Phys. Chem. B* **1997**, *101* (51), 11051-11060.

(20) Shirota, H.; Tamoto, Y.; Segawa, H. Dynamic Fluorescence Probing of the Microenvironment of Sodium Dodecyl Sulfate Micelle Solutions: Surfactant Concentration Dependence and Solvent Isotope Effect. *J. Phys. Chem. A* **2004**, *108* (16), 3244-3252.

(21) Dutt, G. B. Comparison of Microenvironments of Aqueous Sodium Dodecyl Sulfate Micelles in the Presence of Inorganic and Organic Salts: A Time-Resolved Fluorescence Anisotropy Approach. *Langmuir* **2005**, *21* (23), 10391-10397.

(22) Chakrabarty, D.; Chakraborty, A.; Seth, D.; Hazra, P.; Sarkar, N. Effect of Alkyl Chain Length and Size of the Headgroups of the Surfactant on Solvent and Rotational Relaxation of Coumarin 480 in Micelles and Mixed Micelles. *J. Chem. Phys.* **2005**, *122* (18), 184516.

(23) Grant, C. D.; Steege, K. E.; Bunagan, M. R.; Castner, E. W. Microviscosity in Multiple Regions of Complex Aqueous Solutions of Poly(ethylene oxide)-Poly(Propylene oxide)-Poly(ethylene oxide). *J. Phys. Chem. B* **2005**, *109* (47), 22273-22284.

(24) Kumbhakar, M.; Mukherjee, T.; Pal, H. Effect of Added Electrolytes, NaCl and LiCl, on the Palisade Layer Water Structure of Triton X-100 Micelle: A Fluorescence Anisotropy Study. *Chem. Phys. Lett.* **2005**, *413* (1-3), 142-146.

(25) Shiraishi, Y.; Inoue, T.; Hirai, T. Local Viscosity Analysis of Triblock Copolymer Micelle with Cyanine Dyes as a Fluorescent Probe. *Langmuir* **2010**, *26* (22), 17505-17512.

(26) Anand, U.; Mukherjee, S. Microheterogeneity and Microviscosity of F127 Micelle: The Counter Effects of Urea and Temperature. *Langmuir* **2014**, *30* (4), 1012-1021.

(27) Sonu; Kumari, S.; Saha, S. K. Solvation Dynamics and Rotational Relaxation of Coumarin 153 in Mixed Micelles of Triton X-100 and Cationic Gemini Surfactants: Effect of Composition and Spacer Chain Length of Gemini Surfactants. *Phys. Chem. Chem. Phys.* **2016**, *18* (3), 1551-1563.

(28) Ono, J.; Takada, S.; Saito, S. Couplings between Hierarchical Conformational Dynamics from Multi-Time Correlation Functions and Two-Dimensional Lifetime Spectra: Application to Adenylate Kinase. *J. Chem. Phys.* **2015**, *142* (21), 212404.

(29) Kim, K.; Saito, S. Multiple Length and Time Scales of Dynamic Heterogeneities in Model Glass-Forming Liquids: A Systematic Analysis of Multi-Point and Multi-Time Correlations. *J. Chem. Phys.* **2013**, *138* (12), 12A506.

(30) Verma, S. D.; Vanden Bout, D. A.; Berg, M. A. When is a Single Molecule Homogeneous? A Multidimensional Answer and Its Application to Molecular Rotation near the Glass Transition. *J. Chem. Phys.* **2015**, *143*, 024110.

(31) Guo, Z.; Giokas, P. G.; Cheshire, T. P.; Williams, O. F.; Dirkes, D. J.; You, W.; Moran, A. M. Communication: Uncovering Correlated Vibrational Cooling and Electron Transfer Dynamics with Multidimensional Spectroscopy. *J. Chem. Phys.* **2016**, *145* (10), 101101.

(32) Phelps, C.; Israels, B.; Marsh, M. C.; von Hippel, P. H.; Marcus, A. H. Using Multiorder Time-Correlation Functions (TCFs) to Elucidate Biomolecular Reaction Pathways from Microsecond Single-Molecule Fluorescence Experiments. *J. Phys. Chem. B* **2016**, *120* (15), 13003–13016.

(33) Kaur, H.; Verma, S. D.; Paeng, K.; Kaufman, L. J.; Berg, M. A. Biphasic Rate Exchange in Supercooled *o*-Terphenyl from an Ensemble Analysis of Single-Molecule Data. *Phys. Rev. E* **2018**, *98* (4), 040603(R).

(34) Berg, M. A.; Kaur, H. Non-Parametric Analysis of Nonexponential and Multidimensional Kinetics: I. Quantifying Rate Dispersion, Heterogeneity and Exchange. *J. Chem. Phys.* **2017**, *146* (5), 054104.

(35) Verma, S. D.; Corcelli, S. A.; Berg, M. A. Rate and Amplitude Heterogeneity in the Solvation Response of an Ionic Liquid. *J. Phys. Chem. Lett.* **2016**, *7*, 504–508.

(36) Berg, M. A.; Darvin, J. R. Measuring the Dynamics of a Hidden Coordinate: Rate Exchange from 3D Correlation Functions. *J. Chem. Phys.* **2016**, *145* (5), 054119.

(37) Berg, M. A. Multidimensional Incoherent Time-Resolved Spectroscopy and Complex Kinetics. *Adv. Chem. Phys.* **2012**, *150*, 1–102.

(38) Wu, H.; Berg, M. A. Two-Dimensional Anisotropy Measurements Show Local Heterogeneity in a Polymer Melt. *J. Phys. Chem. Lett.* **2014**, *5* (15), 2608–2612.

(39) Sahu, K.; Wu, H.; Berg, M. A. Rate Dispersion in the Biexciton Decay of CdSe/ZnS Nanoparticles from Multiple Population-Period Transient Spectroscopy. *J. Am. Chem. Soc.* **2013**, *135* (3), 1002–1005.

(40) Fleming, G. R. *Chemical Applications of Ultrafast Spectroscopy*. Oxford University Press: Oxford, 1986.

(41) Horng, M. L.; Gardecki, J. A.; Maroncelli, M. Rotational Dynamics of Coumarin 153: Time-Dependent Friction, Dielectric Friction, and Other Nonhydrodynamic Effects. *J. Phys. Chem. A* **1997**, *101* (6), 1030-1047.

(42) Somoza, M. M.; Sluch, M. I.; Berg, M. A. Torsional Relaxation and Friction on the Nanometer Length Scale: Comparison of Small-Molecule Rotation in Poly(dimethylsiloxane) and Poly(isobutylene). *Macromolecules* **2003**, *36* (8), 2721-2732.

(43) Rumble, C. A.; Uitvlugt, C.; Conway, B.; Maroncelli, M. Solute Rotation in Ionic Liquids: Size, Shape, and Electrostatic Effects. *J. Phys. Chem. B* **2017**, *121* (19), 5094-5109.

(44) Kinosita, K.; Kawato, S.; Ikegami, A. A Theory of Fluorescence Polarization Decay in Membranes. *Biophys. J.* **1977**, *20* (3), 289-305.

(45) Halle, B.; Wennerström, H. Interpretation of Magnetic Resonance Data from Water Nuclei in Heterogeneous Systems. *J. Chem. Phys.* **1981**, *75* (4), 1928-1943.

(46) Szabo, A. Theory of Fluorescence Depolarization in Macromolecules and Membranes. *J. Chem. Phys.* **1984**, *81* (1), 150-167.

(47) Bañuelos Prieto, J.; López Arbeloa, F.; Martínez Martínez, V.; Arbeloa López, T.; López Arbeloa, I. Photophysical Properties of the Pyrromethene 597 Dye: Solvent Effect. *J. Phys. Chem. A* **2004**, *108* (26), 5503-5508.

(48) Montejano, H. A.; Amat-Guerri, F.; Costela, A.; García-Moreno, I.; Liras, M.; Sastre, R. Triplet-State Spectroscopy of Dipyrromethene·BF_2 Laser Dyes. *J. Photochem. Photobiol. A* **2006**, *181* (2–3), 142-146.

(49) Costela, A.; García-Moreno, I.; Pintado-Sierra, M.; Amat-Guerri, F.; Sastre, R.; Liras, M.; Arbeloa, F. L.; Prieto, J. B.; Arbeloa, I. L. New Analogues of the BODIPY Dye PM597: Photophysical and Lasing Properties in Liquid Solutions and in Solid Polymeric Matrices. *J. Phys. Chem. A* **2009**, *113* (28), 8118-8124.

(50) Quina, F. H.; Nassar, P. M.; Bonilha, J. B. S.; Bales, B. L. Growth of Sodium Dodecyl Sulfate Micelles with Detergent Concentration. *J. Phys. Chem.* **1995**, *99* (46), 17028-17031.

(51) Bergström, M.; Skov Pedersen, J. Structure of Pure SDS and DTAB Micelles in Brine Determined by Small-Angle Neutron Scattering (SANS). *Phys. Chem. Chem. Phys.* **1999**, *1* (18), 4437-4446.

(52) Hammouda, B. Temperature Effect on the Nanostructure of SDS Micelles in Water. *J. Res. Natl. Inst. Stand. Technol.* **2013**, *118*, 151-167.

(53) Gubaidullin, A. T.; Litvinov, I. A.; Samigullina, A. I.; Zueva, O. S.; Rukhlov, V. S.; Idiyatullin, B. Z.; Zuev, Y. F. Structure and Dynamics of Concentrated Micellar Solutions of Sodium Dodecyl Sulfate. *Russ. Chem. Bull.* **2016**, *65* (1), 158-166.

(54) Missel, P. J.; Mazer, N. A.; Benedek, G. B.; Carey, M. C. Influence of Chain Length on the Sphere-to-Rod Transition in Alkyl Sulfate Micelles. *J. Phys. Chem.* **1983**, *87* (7), 1264-1277.

(55) Bezzobotnov, V. Y.; Borbely, S.; Cser, L.; Farago, B.; Gladkih, I. A.; Ostanevich, Y. M.; Vass, S. Temperature and Concentration Dependence of Properties of Sodium Dodecyl Sulfate Micelles Determined from Small Angle Neutron Scattering Experiments. *J. Phys. Chem.* **1988**, *92* (20), 5738-5743.

(56) Istratov, A. A.; Vyvenko, O. F. Exponential Analysis in Physical Phenomena. *Rev. Sci. Instrum.* **1999**, *70* (2), 1233-1257.

(57) Johnson, N. L.; Kotz, S.; Balakrishnan, N. *Continuous Univariate Distributions*. John Wiley & Sons: New York, 1995; Vol. 2.

Supporting Information for "Micelle Heterogeneity from the 2D Kinetics of Solute Rotation"

Jason R. Darvin and Mark A. Berg

Department of Chemistry and Biochemistry, University of South Carolina, Columbia, SC 29208, USA

■ EXPERIMENTAL METHODS

Sample. The sample consisted of an aqueous solution of sodium dodecyl sulfate (SDS, 200 mM) and pyrromethene 597 (PM597, 52 μM) in a 1.0 mm flow cell at 22 °C (see Figure S1). The solution had an optical density of 0.39 at the excitation wavelength of 530 nm. At this concentration, the SDS forms micelles containing ~80 molecules.[50-55] The micelles are crowded enough to have correlations in the inter-micelle positions, but they are not crowded enough to perturb the internal structure of the micelles. To confirm this conclusion, 1D measurements at SDS concentrations of 150 mM and 100 mM with the same dye concentration were made, but showed no difference from the 200 mM sample.

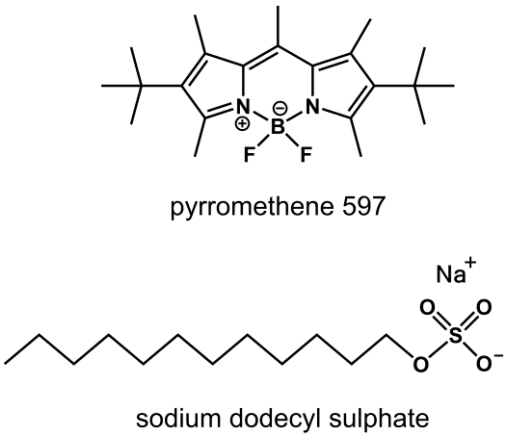

Figure S1. Structures of pyrromethene 597 (PM597) and sodium dodecyl sulfate (SDS).

PM597 has simple photochemistry: high quantum yield, low triplet yield, weak excited-state absorption, good photostability and weak solvatochromism.[47-49] The sample had an average of one PM597 molecule per 46 micelles, so dye interactions are not expected. To confirm this expectation, the dye concentration was varied to give sample optical densities between 0.17–0.64. No effect on the 1D measurements was found. PM597 is poorly soluble in water: a saturated

solution has an optical density of 8×10^{-4} in 1.0 mm. The signal from PM597 independent of a micelle can be neglected.

Optical system. The laser pulses were generated by a standard, 1-kHz Ti:sapphire laser system. The signal from a white-light-seeded optical parametric generator was mixed with 800 nm pulses to generate pulses at 530 nm with a bandwidth of 150 cm^{-1}. At the sample, the pulses had a length of ~300 fs (not bandwidth limited) and an energy of 80 nJ/pulse.

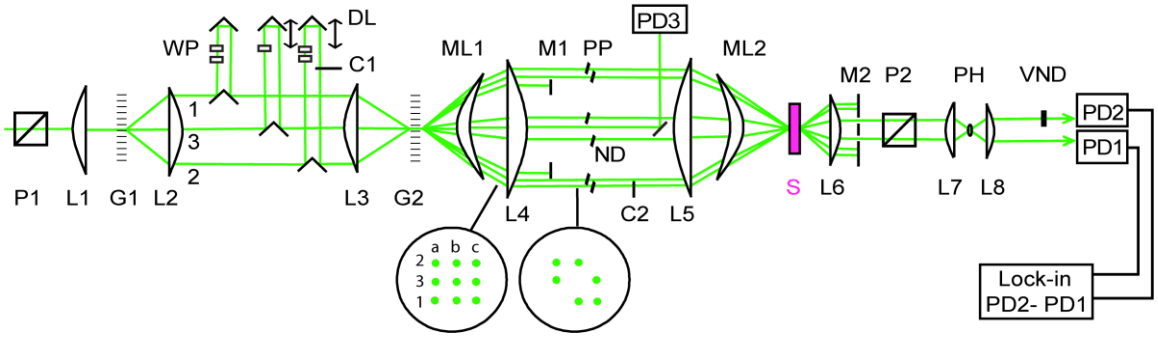

Figure S2. MUPPETS optical system: polarizers (P), lenses (L), transmission gratings (G), delay lines (DL), meniscus lenses (ML), phase plates (PP), neutral density filter (ND), masks (M), sample (S), pinhole (PH), and photodiodes (PD).

The MUPPETS current optical system is shown in Figure S2. Its design and operation have been described in detail elsewhere.[37-38] The initial pulse is split equally in the vertical direction into first excitation (1), second excitation (2), and probe (3) by a transmission grating (G1). Waveplates (WP) and polarizer P2 were used to adjust the polarizations at the sample to the required combinations (Figure S4a). Extinction ratios were in the range 500–5000 at the sample. A second grating (G2) further divided the pulses into nine equal intensity pulses (Figure S2, left cross-section). Three pulses were blocked to leave the six pulses used for the experiment (Figure S2, right cross-section). The differential heterodyne detection required unequal probe intensities at the sample.[S1] One of the phase plates was also a neutral density filter (ND, optical density 1.0, pulse 3c). A compensating variable neutral density (VND) filter was placed in beam 3a.

In polarization measurements, it is common to make a "G-factor" correction by matching the tails of the signals at long times, when rotation is complete. Because those times lie outside our 2-ns time window, we made several changes to the MUPPETS set-up to improve its stability across multiple scans: (1) Fine angle adjustments were added to lens L5 to correct for residual coma. (2) A magnifying doublet lens and camera (not shown) were used to image the beams at the sample position. This system can detect self-focusing, spherical aberration, horizontal and vertical coma, and horizontal and vertical astigmatism. Each of these problems can be systematically corrected by appropriate adjustments of the main (L4, L5) and meniscus (ML1, ML2) lenses. (3) A slow

response (300 ms) photodiode (PD3) independently measured fluctuations in the laser power, which were used to correct both 1D and 2D measurements. (4) Phase plates (PP) have been added to all the beams to allow phase shifts in the excitations.

It was found that residual signal from low-order processes were a significant cause of long term drift and instability, so additional measures were taken to remove them by fast modulation. The first excitation and probe were amplitude modulated by two choppers. The second excitation (2a and 2b) was modulated by chopper C1; pulse 1c was modulated by chopper C2. Both choppers operated at 250 Hz, but with a 90° phase shift, that is, shifted by one pulse period. The signal was detected at 500 Hz with the phase set to give no signal when the pulse 1c was blocked.

1D measurements. Pump–probe measurements out to 2 ns were made on the same system using pulses 1c and 3c. The raw data are shown in Figure S3. The time range was extended using measurements by time-correlated single-photon counting (150 ps FWHM instrument response function, 373 nm excitation, 560 nm detection) on a sample with an optical density of 0.10. Anisotropy results for times >700 ps and electronic results for times >1 ns were matched to the pump–probe data in the overlapping regions to create data sets over times from 1 ps – 10 ns. Measurements were taken at parallel $\Delta A_{\parallel}(\tau)$, perpendicular $\Delta A_{\perp}(\tau)$ and magic-angle $\Delta A_{\mathrm{m}}(\tau)$ polarizations. The amplitudes of the parallel and perpendicular decays were adjusted slightly to match the sum to the magic-angle results before calculating the anisotropy.

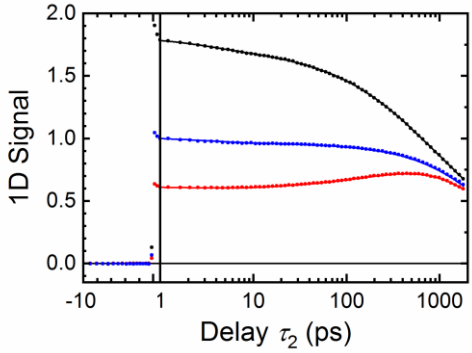

Figure S3. The raw, 1D pump–probe data for PM597 in SDS micelles: parallel ($\Delta A_{\parallel}(\tau)$, black), perpendicular ($\Delta A_{\perp}(\tau)$, red), and magic-angle ($\Delta A_{\mathrm{m}}(\tau)$, blue) polarizations. The scale changes from linear for times <1 ps to logarithmic for times >1 ps. Data are shown as points, and fits to eq 16 are shown as solid lines.

2D measurements. The 2D signal $\Delta A_p(\tau_2, \tau_1; \varphi)$ is a change in absorbance as a function of two time separations, τ_1 and τ_2, phase φ and polarization conditions p. This signal was recorded as sets of scans along τ_2 at a fixed value of τ_1. Scans were taken at each of the four polarization combinations shown in Figure S4a. The (++/−−) and (+−/−+) pairs should be identical. All four

polarizations were measured to check for consistency and to improve averaging. The phase of the second excitation (beam 2b) was adjusted for either maximum positive (0°) or maximum negative (180°) signal. Measurements at other phases at τ_1 = 1 ps showed a constant phase, so only these two phases were needed. All polarizations were measured at both phases, giving a total of eight scans in a set (Figure S4b). These scans were combined to give

$$\begin{aligned}\Delta A_{++}(\tau_2,\tau_1) = \Delta A_{++}(\tau_2,\tau_1;0°) - \Delta A_{++}(\tau_2,\tau_1;180°) \\ +\Delta A_{--}(\tau_2,\tau_1;0°) - \Delta A_{--}(\tau_2,\tau_1;180°)\end{aligned} \tag{12}$$

and

$$\begin{aligned}\Delta A_{+-}(\tau_2,\tau_1) = \Delta A_{+-}(\tau_2,\tau_1;0°) - \Delta A_{+-}(\tau_2,\tau_1;180°) \\ +\Delta A_{-+}(\tau_2,\tau_1;0°) - \Delta A_{-+}(\tau_2,\tau_1;180°),\end{aligned} \tag{13}$$

which are shown in Figure S4c.

Because each set was typically taken on a separate day, their amplitudes and noise levels varied. To correct this variation, a preliminary, multiexponential fit (eq 16) was made to each fixed-τ_1 curve to extract initial values, $\Delta A_{++}(1\text{ps}, \tau_1)$ and $\Delta A_{+-}(1\text{ps}, \tau_1)$, and residuals. The chi-squared values of the residuals were used to weight the later fitting. The amplitude of $\Delta A_{++}(\tau_2, \tau_1)$ and $\Delta A_{+-}(\tau_2, \tau_1)$ were individually adjusted to match the τ_1 = 1 ps scan, assuming τ_1–τ_2 symmetry, $\Delta A_p(\tau_2, 1\text{ps}) = \Delta A_p(1\text{ps}, \tau_1)$. These adjustment effectively combine sequences of 1D slices into unified, 2D surfaces.

The weighted sum of $\Delta A_{++}(\tau_2, \tau_1)$ and $\Delta A_{+-}(\tau_2, \tau_1)$ (eq 10) formed the electronic–electronic decays shown in Figures S4d and 2a. For homogeneous electronic relaxation, the 2D result can be predicted from the 1D results:

$$C_{\text{ee}}^{(2)}(\tau_2,\tau_1) = C_{\text{e}}^{(1)}(\tau_2)C_{\text{e}}^{(1)}(\tau_1) \tag{14}$$

(solid curves in Figure 2a, Table S2). These results matched the data. Because the 1D results are more accurate, the results of eq 14 were used in eq 18 and to corrected the anisotropy–anisotropy results (eq 15) to the rotation–rotation decay (eq 10).

The difference of $\Delta A_{++}(\tau_2, \tau_1)$ and $\Delta A_{+-}(\tau_2, \tau_1)$ is the 2D anisotropy–anisotropy decay,

$$C_{\text{aa}}^{(2)}(\tau_2,\tau_1) = \frac{\Delta A_{++}(\tau_2,\tau_1) - \Delta A_{+-}(\tau_2,\tau_1)}{\frac{7}{12}\Delta A_{++}(0,0) + \frac{5}{12}\Delta A_{+-}(0,0)}. \tag{15}$$

An example is shown in Figure S4d. In the end, the anisotropy–anisotropy decay is divided by the electronic–electronic decay to give the rotation–rotation decay (eq 10, Figure 2b). However, all the intermediate data reduction was done on this anisotropy–anisotropy decay.

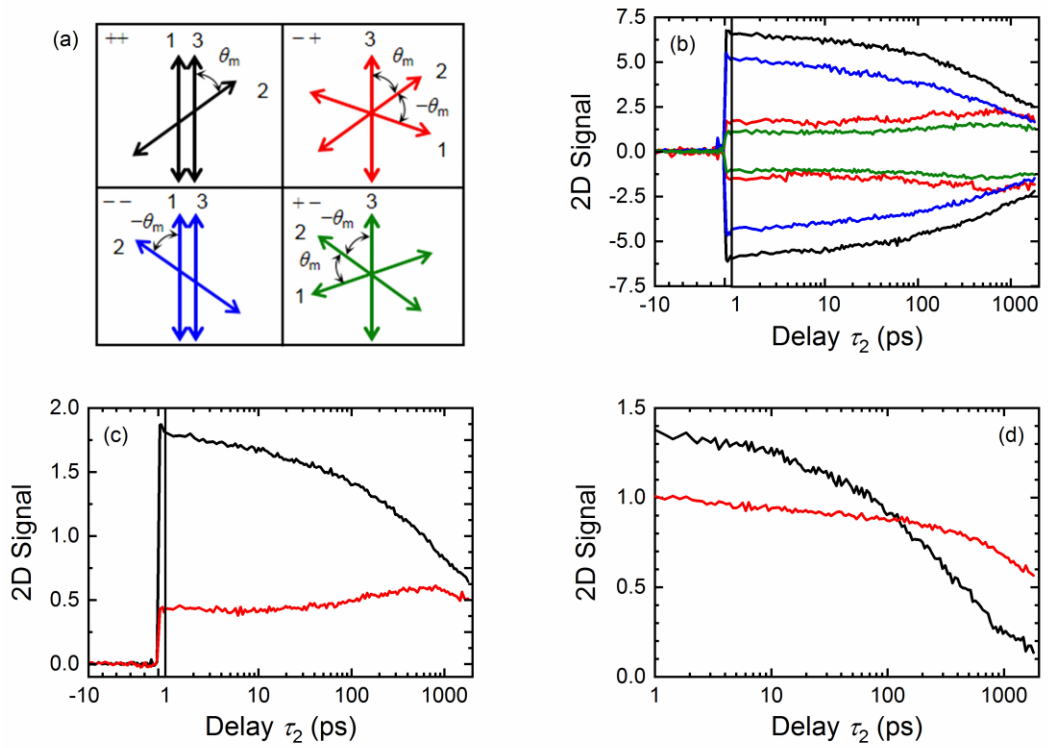

Figure S4. The MUPPETS data for τ_1 = 1 ps. (a) The polarization of the first (1) and second (2) excitations and of the probe (3) are separated by the magic angle θ_m [measured relative to (2)] to create four polarization combinations. (b) The raw data $\Delta A_p(\tau_2, \tau_1; \varphi)$ with colors corresponding to the polarization conditions in (a). Positive and negative signals correspond to 0° and 180 phases, respectively. (c) The signals $\Delta A_{++}(\tau_2, \tau_1)$ (black) and $\Delta A_{--}(\tau_2, \tau_1)$ (red) are derived by combining the results in (a) (eqs 12 and 13). (d) The signals from (c) are added to give the electronic–electronic decay $C_{ee}^{(2)}(\tau_2,\tau_1)$ (eq 9, red) or subtracted to give the anisotropy–anisotropy decay $C_{aa}^{(2)}(\tau_2,\tau_1)$ (eq 15, black). The time scales in (b) and (c) change from linear for times <1 ps to logarithmic for times >1 ps.

■ NONPARAMETRIC DATA REDUCTION

1D spectrum. The 1D anisotropy and electronic decay data were each fit to

$$C_{a/e}^{(1)}(\tau_1) = \sum_{i=0}^{N} \tilde{c}_{a/e,i}^{(1)} \exp\left(-\tau_1/T_i\right) \tag{16}$$

with fixed $T_i = 4^i \times 2$ ps. For the anisotropy decay, N = 5; for the electronic decay, N = 7. The fits are shown in Figure S3 and the values of $\tilde{c}_{a/e,i}^{(1)}$ are given in Table S1.

This fit does not have physical significance; it only encodes our expectation that the signal decays smoothly and monotonically. Hundreds of data points containing both signal and noise are reduced to a few coefficients representing the signal. Residuals from the fit represent the noise

that is removed when the number of degrees of freedom is reduced. The chi-squared of the fit could be decreased further by decreasing the spacing of the T_i and increasing the number of $\tilde{c}^{(1)}_{\mathrm{a/e},i}$. However, we would start "fitting the noise"; the result would be less smooth and would include more noise.

This fit was used to calculate the 1D rate spectrum (eq 3), and this spectrum is further reduced to the final parameters, $\overline{T}_{\mathrm{r}}$ and d_{rot}. Although eq 16 is a specific functional form, it is chosen only for mathematical convenience, and it is only used as an intermediate representation of the signal. Any other form that goes through the data equally well would give indistinguishable spectra and final parameters.

The set of $\tilde{c}^{(1)}_{\mathrm{a/e},i}$ can be regarded as a rate spectrum of the data. However, rate spectra are never unique and many other spectra would represent the data equally well. For example, the later part of the electronic decay is well fit by a single exponential with a 4.8 ns time constant. The negative coefficients at 512 and 32,768 ps are the result of representing it with exponentials with different, fixed time constants.

Table S1. Coefficients Summarizing the 1D Anisotropy and Electronic Decays[a]

T_i (ps)	2	8	32	128	512	2048	8192	32,768
Anisotropy [b]	−0.009	0.051	0.029	0.201	0.514	0.214	—	—
Electronic [c]	0.050	0.007	0.005	0.012	−0.001	0.295	0.824	−0.192

[a] See eq 16. [b] $\tilde{c}^{(1)}_{\mathrm{a},i}$ [c] $\tilde{c}^{(1)}_{\mathrm{e},i}$

Initial 2D spectrum. A similar procedure was applied to the 2D anisotropy, but with the 2D extension of eq 16:

$$C^{(2)}_{\mathrm{aa}}(\tau_2,\tau_1) = \sum_{\substack{j,i=0 \\ j>i}}^{5} \tilde{c}^{(2)}_{\mathrm{aa},ij}\Big[\exp\left(-\tau_2/T_j\right)\exp\left(-\tau_1/T_i\right) + \exp\left(-\tau_2/T_i\right)\exp\left(-\tau_1/T_j\right)\Big] + \sum_{i=0}^{5} \tilde{c}^{(2)}_{\mathrm{aa},ii}\exp\left(-\tau_2/T_i\right)\exp\left(-\tau_1/T_i\right) \quad . \tag{17}$$

Symmetry in τ_2–τ_1 and in the resulting coefficient matrix is enforced, $\tilde{c}^{(2)}_{\mathrm{a},ij} = \tilde{c}^{(2)}_{\mathrm{a},ji}$, reducing the number of degrees of freedom to 21. Ultimately, the 2D measurement holds only one piece of new information, the degree of heterogeneity. Thus, even reducing the data to 21 degrees of freedom still leaves significant flexibility.

The fit was done with singular-value decomposition, which allows the number of degrees of freedom to be systematically reduced by setting large singular values to zero.[S2] The fitting procedure forces the corresponding linear combinations of the $\tilde{c}^{(1)}_{\mathrm{a},i}$ to zero, creating a smoother spectrum at the expense of a higher chi-squared. Whether the higher chi-squared represents a loss of fidelity to the signal or a greater rejection of noise relies on the judgement of the analyst.

The 2D anisotropy–anisotropy spectrum with eight degrees-of-freedom is shown in Figure S5. Two features are evident. The main peak is strongly elongated along the diagonal, indicating strong rate heterogeneity. In addition, there are weak cross-peaks near (2 ps, 2 ns). These cross-peaks could be due to leakage of electronic–electronic signal into the anisotropy–anisotropy measurements. The electronic–electronic spectrum has similar cross-peaks between the fast solvation process and the slow electronic state lifetime. The polarization conditions were calculated for collinear beams, whereas in the experiment, the beams intersect at angles up to 3° from the center line, slightly modifying the correct polarization angles. This systematic error could allow electronic–electronic signal to leak into our anisotropy measurements.

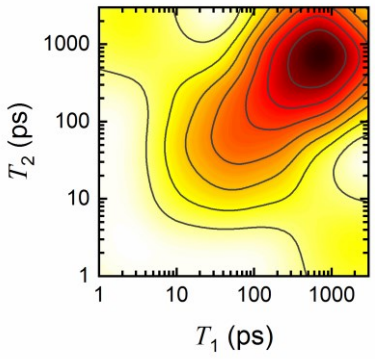

Figure S5. The 2D anisotropy–anisotropy decay spectrum from the initial fitting to eq 17 with eight degrees of freedom.

Refined 2D spectrum. These observations led us to a more refined fitting procedure that allows us to include more of our theoretical expectations. We used this function:

$$
\begin{aligned}
C^{(2)}_{\mathrm{aa}}(\tau_2,\tau_1) = {} & A_{\mathrm{a}} \sum_{i=0}^{5} \tilde{c}^{(1)}_{\mathrm{a},i} \tilde{c}^{(1)}_{\mathrm{a},i} \exp\left(-\tau_2/T_i\right) \exp\left(-\tau_1/T_i\right) \\
& + A_{\mathrm{e}} \sum_{j,i=0}^{7} \tilde{c}^{(2)}_{\mathrm{ee},ij} \left[\exp\left(-\tau_2/T_j\right) \exp\left(-\tau_1/T_i\right) \right] \\
& + \sum_{j=\max(0,i-1)}^{\min(5,i)} \sum_{i=0}^{5} \delta\tilde{c}^{(2)}_{\mathrm{aa},ij} \left[\exp\left(-\tau_2/T_j\right) \exp\left(-\tau_1/T_i\right) + \exp\left(-\tau_2/T_i\right) \exp\left(-\tau_1/T_j\right) \right] \qquad (18)
\end{aligned}
$$

The first line represents a fully heterogeneous anisotropy spectrum, as predicted from the 1D data. Using this term incorporates our expectation that the 1D and 2D spectra are consistent with each other. Using this term alone ($A_e = 0$, $\delta\tilde{c}^{(2)}_{e,ij} = 0$), leaves only one degree of freedom in the fit, the amplitude A_a. It gives the chi-squared shown by the green square in Figure S6.

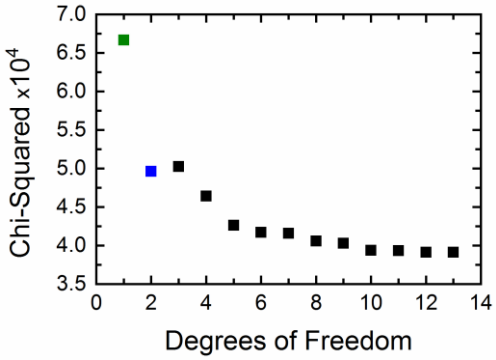

Figure S6. Chi-squared versus the number of degrees of freedom for the refined fit to the 2D data (eq 18). Green (1 deg. freedom): for the 100% heterogeneous model. Blue (2 deg. freedom): with electronic–electronic leakage added. Black: with homogeneous broadening added.

The second term represents leakage of the electronic–electronic signal. The coefficients $\tilde{c}^{(2)}_{ee,ij}$ are already determined, so only the amplitude A_e is varied. Adding this degree of freedom reduces the chi-squared significantly (blue square in Figure S6) with a small A_e .

The third term in eq 18 creates deviations from heterogeneous behavior. The coefficients $\delta\tilde{c}^{(2)}_{aa,ij}$ allow intensity to move from the diagonal regions to off-diagonal ones. Because the central peak is expected to broaden, the transfer was limited to near-diagonal regions of the spectrum, that is, to next-to-diagonal coefficients. Attempts to include coefficient farther from the diagonal did not improve the fit.

The coefficients $\delta\tilde{c}^{(2)}_{aa,ij}$ were fit while the amplitudes A_a and A_e were fixed at their previously determined values. The procedure was then iterated: The fit to A_a and A_e was repeated with fixed $\delta\tilde{c}^{(2)}_{aa,ij}$ (giving a final result, A_e = 4.7%) and then the $\delta\tilde{c}^{(2)}_{aa,ij}$ were refit with fixed A_a and A_e. The reiteration gave only a small change.

The squares in Figure S6 shows the value of chi-squared with the number of degrees of freedom in the final fit. The spectrum in Figure 3b and the remaining analysis were based on the fit with five degrees of freedom. Based purely on measures internal to the data set, chi-squared and number of degrees of freedom, this description of the data is equivalent to the initial spectrum in Figure S5. However, the refined fit better incorporates external information: it gives a vertical projection that is in better agreement with the 1D kinetics (Figure 1b), it allows for leakage of the

electronic–electronic signal, and the horizontal projection has quickly decaying tails that lie between the limiting heterogeneous and homogeneous limits (Figure 3d).

Table S2. Coefficients Summarizing the 2D Anisotropy–Anisotropy (top[a]) and Electronic–Electronic (bottom[b]) Decays.

T_j (ps) \ T_i (ps)	2	8	32	128	512	2048	8192	32,768
2	−0.003 0.003	0.002 0.000	— 0.000	— 0.001	— 0.000	— 0.015	— 0.042	— −0.010
8	0.002 0.000	0.044 0.000	0.031 0.000	— 0.000	— 0.000	— 0.002	— 0.005	— −0.001
32	— 0.000	0.031 0.000	−0.006 0.000	0.036 0.000	— 0.000	— 0.001	— 0.004	— −0.001
128	— 0.001	— 0.000	0.036 0.000	0.119 0.000	0.031 0.000	— 0.004	— 0.010	— −0.002
512	— 0.000	— 0.000	— 0.000	0.031 0.000	0.437 0.000	−0.003 0.000	— −0.001	— 0.000
2048	— 0.015	— 0.002	— 0.001	— 0.004	−0.003 0.000	0.205 0.087	— 0.243	— −0.057
8192	— 0.042	— 0.005	— 0.004	— 0.010	— −0.001	— 0.243	— 0.679	— −0.158
32,768	— −0.010	— −0.001	— −0.001	— −0.002	— 0.000	— −0.057	— −0.158	— 0.037

[a] $\tilde{c}^{(2)}_{\mathrm{aa},ij} = \tilde{c}^{(1)}_{\mathrm{a},i}\tilde{c}^{(1)}_{\mathrm{a},j} + \delta\tilde{c}^{(2)}_{\mathrm{aa},ij}$. See eq 18. [b] $\tilde{c}^{(2)}_{\mathrm{ee},ij} = \tilde{c}^{(1)}_{\mathrm{e},i}\tilde{c}^{(1)}_{\mathrm{e},j}$. See eq 14.

■ APPROXIMATING THE MICROVISCOSITY DISTRIBUTION

The convolution inherent in kinetic measurements results in a loss of information (eq 7), so the 1D decay spectrum (Figure 1b) cannot be uniquely decomposed into its homogeneous and heterogeneous contributions. Fortunately, the loss of information is not complete, and a representative decomposition can be made to illustrate the retained information. The low-order moments of it can be recovered accurately; the loss of information primarily affects higher moments.

The process uses cumulants κ_n, which are combination of moments.[S3] They are additive under convolution. Thus from eq 7,

$$\kappa_n[\hat{C}^{(1)}_{\mathrm{r}}] = \kappa_n[\hat{C}_{\mathrm{hom}}] + \kappa_n[P_{\mathrm{het}}] \tag{19}$$

holds for the decay spectra. The connection between rate and decay spectra (eq 5) leads to

$$\kappa_n[\hat{C}^{(1)}] = \kappa_n[\tilde{C}^{(1)}] + \kappa_n[\hat{C}^{(1)}_{\mathrm{exp}}]. \tag{20}$$

Combining these equations gives a relationship between rate spectra,

$$\kappa_n[\tilde{C}_{\mathrm{r}}^{(1)}] = \kappa_n[\tilde{C}_{\mathrm{hom}}] * \kappa_n[P_{\mathrm{het}}]. \tag{21}$$

The rate spectrum of the 1D rotational decay is easy to find from the form used to represent it, eq 16. We believe that the first four cumulants are meaningful. They are given in Table S3.

To provide a specific model, the homogeneous decay was taken to be a biexponential,

$$C_{\mathrm{hom}}(x) = \tfrac{1}{2}(1+b)e^{-x/x_-} + \tfrac{1}{2}(1-b)e^{-x/x_+}. \tag{22}$$

with a geometric-mean (first moment) of zero. The heterogeneous distribution is assumed to be a smooth, single-peaked function. It should also have sharply defined maximum and minimum values, because the micelle should have well-defined maximum and minimum viscosities. The beta distribution satisfies these criteria and can be easily adjusted to have the desired first four moments.[57] It was used to model the heterogeneous distribution,

$$P_{\mathrm{het}}(\ln T) = \frac{(\ln T - a)^{\alpha-1} + (c - \ln T)^{\beta-1}}{(c-a)^{\alpha+\beta+1}\, B(\alpha,\beta)}, \tag{23}$$

where $B(\alpha,\beta)$ is the beta function. Equation 23 holds for $a < \ln T < c$; the distribution is zero elsewhere.

The assignment of the cumulants proceeds as follows (see Table S3). Because the homogeneous decay is defined to have a zero 1st moment, the heterogeneous distribution takes the first moment of the 1D spectrum. The 2D experiment determined that 87% of the 1D 2nd cumulant (d_{rot}) should be assigned to the heterogeneous second cumulant (d_{het}). The 2nd cumulant of the homogeneous decay is then the remaining 13% of d_{rot}. We assumed that the kurtosis of the heterogeneous distribution (ratio of 4th and 2nd cumulants[S3]) was the same as that of the 1D spectrum. The 4th cumulant of the homogeneous decay was calculated by subtraction. The 1st, 2nd and 4th cumulants of the homogeneous decay completely determine the constants in eq 22: $b = -0.742$, $x_+ = 2.12$, $x_- = 0.550$. From these values, the 3rd moment of the homogeneous decay was calculated and subtracted from the 1D 3rd moment to give the heterogeneous 3rd moment. The first four cumulants of the heterogeneous distribution were then known, so the parameters in eq 23 could be determined:[57] a = ln (1.60 ps), c = ln (1.10 ns), $\alpha = 3.25$, $\beta = 1.03$.

Table S3. Cumulants Calculated on a Ln-T Scale

spectrum	κ_1	κ_2	κ_3	κ_4
rotational rate [a]	5.433	1.575	−1.633	7.946
homogenous rate [b]	—	0.205	−0.205	0.247
heterogeneous rate [c]	5.433	1.371	−1.427	6.014

[a] $\tilde{C}_{\mathrm{r}}^{(1)}(\ln T)$ [b] $\tilde{C}_{\mathrm{hom}}^{(1)}(\ln T)$ [c] $P_{\mathrm{het}}(\ln T)$

The rotation time of PM597 was measured in a number of solvents, as shown in Figure S7. All the decays were close to single exponential. The figure reports geometric-mean times versus viscosities. The results were fit to $\overline{T}_r = B\eta$, with B = 31.6 ps/cP. This formula was used to generate the microviscosity scale in Figure 4.

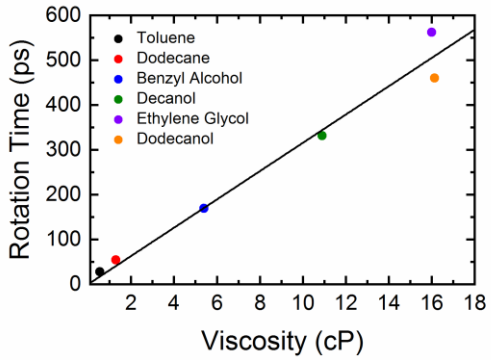

Figure S7. The geometric-mean rotation time $\overline{T}_r$ of PM597 in various solvents versus their macroscopic viscosities η (points) and a linear fit (line).

■ REFERENCES

(S1) Khurmi, C.; Berg, M. A. Differential Heterodyne Detection with Diffractive Optics for Multidimensional Transient-Grating Spectroscopy. *J. Opt. Soc. Am. B* **2009**, *26* (12), 2357–2362

(S2) Press, W. H.; Teukolsky, S. A.; Vetterling, W. T.; Flannery, P. P. *Numerical Recipes in C*. Second ed.; Cambridge University Press: Cambridge, 1992.

(S3) Stuart, A.; Ord, J. K. *Kendall's Advanced Theory of Statistics*. Oxford University Press: New York, 1987; Vol. 1.